Black Tungsten Oxide Nanofiber as a Robust Support for Metal Catalysts: High Catalyst Loading for Electrochemical Oxygen Reduction

*Ga-Yoon Kim, Ki Ro Yoon, Kihyun Shin, Ji-Won Jung, Graeme Henkelman, and Won-Hee Ryu**

Black valve metal oxides with low oxygen vacancies are identified to be promising for various industrial applications, such as in gas sensing, photocatalysis, and rechargeable batteries, owing to their high reducibility and stability, as well as considerable fractions of low-valent metal species and oxygen vacancies in their lattices. Herein, the nanofiber (NF) of black oxygen-deficient tungsten trioxide (WO_{3-x}) is presented as a versatile and robust support for the direct growth of a platinum catalyst for oxygen reduction reaction (ORR). The nonstoichiometric, poorly crystallized black WO_{3-x} NFs are prepared by electrospinning the W precursor into NFs followed by their low-temperature (650 °C) reductive calcination. The black WO_{3-x} NFs have adequate electrical conductivity owing to their decreased bandgap and amorphous structure. Remarkably, the oxygen-deficient surface (surface O/W = 2.44) facilitates the growth of small Pt nanoparticles, which resist aggregation, as confirmed by structural characterization and computational analysis. The Pt-loaded black WO_{3-x} NFs outperform the Pt-loaded crystalline white WO_{3-x} NFs in both the electrochemical ORR activity and the accelerated durability test. This study can inspire the use of oxygen-deficient metal oxides as supports for other electrocatalysts, and can further increase the versatility of oxygen-deficient metal oxides.

1. Introduction

With growing industrial development and the associated need for innovative materials, there is an increasing demand for developing new synthetic methods and processing techniques to generate new materials. Additionally, it is necessary to modify the existing materials and thus alter their intrinsic properties to overcome their limitations. In particular, the modification of the electrical and chemical properties of metal oxides can pave the way for their widespread application in energy and environmental fields.[1]

One of the promising approaches is to modify metal oxides for use as supports for electrocatalysts.[2] Despite tremendous progress in this direction over the past decades, improving the activity and durability of various electrocatalysts remains a major challenge, which has hindered the commercialization of proton-exchange membrane (PEM) fuel cells. The widely adopted catalyst–support hybrid system, namely, platinum nanoparticles (NPs) dispersed on a carbon black support, has shown the highest activity in oxygen reduction reaction (ORR) in fuel cells. It, however, still suffers from issues such as degradation (especially due to carbon corrosion), dissolution, agglomeration, and/or detachment of the catalytic NPs.[3] Therefore, there is a significant interest in using metal oxides, such as titanium dioxide,[4] cerium oxide,[5] and niobium oxide,[6] as alternative supports owing to their high corrosion resistance, robustness, and potential beneficial chemical interaction with catalytic NPs, termed as strong metal–support interaction.[2b,7] More importantly, the compositional modification and surface structural diversity of such catalyst/metal oxide systems offer myriad options for tuning their electrocatalytic properties.

However, certain issues of metal oxide supports, including their inferior electrical conductivity as compared to that of carbon black and low electrochemical surface area induced by agglomeration during their high-temperature synthesis (>1000 °C), still persist, hindering their widespread utilization. Furthermore, in contrast to nanoporous carbonaceous supports, the direct growth of catalysts on the relatively smooth surface of metal oxides can make the precise control of the size

G.-Y. Kim, W.-H. Ryu
Department of Chemical and Biological Engineering
Sookmyung Women's University
100 Cheongpa-ro 47-gil, Yongsan-gu, Seoul 04310, Republic of Korea
E-mail: whryu@sookmyung.ac.kr
K. R. Yoon
Advanced Textile R&D Department
Korea Institute of Industrial Technology (KITECH) 143
Hanggaul-ro, Sangnok-gu, Ansan-si, Gyeonggi-do 15588
Republic of Korea
K. Shin, G. Henkelman
Department of Chemistry and the Oden Institute
of Computational Engineering and Sciences
University of Texas at Austin
100 E 24th Street A5300, Austin, TX 78712, USA
J.-W. Jung
School of Materials Science and Engineering
University of Ulsan
14, Techno saneop-ro 55 beon-gil, Nam-gu, Ulsan 44776
Republic of Korea

ADVANCED
SCIENCE NEWS
www.advancedsciencenews.com

NANO · MICRO
small
www.small-journal.com

and distribution of catalytic NPs difficult, and therefore, their catalytic potential may not be fully realized.[8]

Black tungsten trioxide (WO_{3-x}) is a well-known metal oxide because of its reducibility. Moreover, its crystalline lattice can tolerate a high concentration of oxygen vacancies and have low-valent tungsten metal species.[9] Oxygen vacancies in the metal oxide serve as shallow donors that can modulate the band structure and aid the formation of defective nonstoichiometric metal oxides, thereby improving the electrical conductivity and donor density, as well as enhancing the surface adsorption properties.[10] Therefore, WO_{3-x} has attracted great attention because of its unusual structural defects and unique surface characteristics, which include i) high electrical conductivity induced by the decreased bandgap, ii) high surface activity, iii) improved ion mobility, and iv) structural flexibility owing to the generation of free volume. This new class of material should extend the utilization of WO_{3-x} in the areas of gas sensing, photocatalysis, rechargeable fuel cells, and others.[7,11] We believe that WO_{3-x} with controlled oxygen deficiency can also serve as a promising support for Pt-based electrocatalysts in fuel cells.

Another critical aspect of the catalyst–support system is the morphological combination of the catalytic nanoparticles and supports, which should possess a high exposure and dispersion degree of catalytic particles on the supporting material as well as facile, fast charge, and mass transfers. In this regard, various 1D fiber-type scaffolds, such as TiO_2, Nb-doped TiO_2, Co_4N fibers, and carbon nanofibers (NFs), have been devised as catalyst-supporting materials in the literature.[2c,12] 1D nanofibers are usually synthesized using solution-based processes, such as hydrothermal reactions,[13] sol–gel routes,[14] and template-assisted multiple steps.[15] However, these methods have a low production yield, and are complicated and possibly lead to low reproducibility.

In this study, we report an efficient strategy for preparing a Pt metal catalyst on a metal oxide support using WO_{3-x} NFs with controlled oxygen deficiency. Various WO_{3-x} NFs were obtained by electrospinning, which is a facile, versatile, and scalable technique for fabricating 1D nanomaterials, followed by calcination at a relatively low temperature (650 °C) under a reducing atmosphere (H_2/Ar). The 1D, poorly crystallized, dark WO_{3-x} NFs (hereafter referred to as black WO_{3-x} NFs) provide a large surface area and stable anchoring sites for the direct growth of Pt NPs, enabling the full utilization of the supported catalyst by limiting the agglomeration of Pt NPs during their formation. The Pt/black WO_{3-x} NF system exhibits outstanding catalytic performance in ORR, better than that of Pt-loaded crystalline white WO_{3-x} NFs obtained by oxidative calcination (650 °C in air) of the electrospun fibers. Based on the structural characterization and computational study, we attribute the high catalytic activity to the enhanced bulk electrical conductivity of the black WO_{3-x} NFs, owing to their reduced optical bandgap (1.48 eV), numerous ORR sites at the size-controlled Pt NPs facilitated by surface oxygen vacancies (O/W_{surf} = 2.44) on the black WO_{3-x} NFs, as well as the favorable surface charge properties of the Pt NPs. The enhanced durability of the Pt/black WO_{3-x} NFs is attributed to strong coupling between the Pt clusters and oxygen-deficient WO_{3-x} surface, and its ability to prevent the aggregation of Pt NPs, thus enabling a high-efficient Pt loading and catalytic durability. This report highlights a novel strategy for the preparation of a high-performance catalyst/metal oxide hybrid, and also provides a new direction for the widespread utilization of metal oxides that overcome their current limitations.

2. Results and Discussion

Figure 1 presents the fabrication procedures for Pt-loaded white WO_{3-x} NFs and black WO_{3-x} NFs. First, we electrospun a solution of tungsten(VI) chloride (WCl_6) and polyvinylpyrrolidone
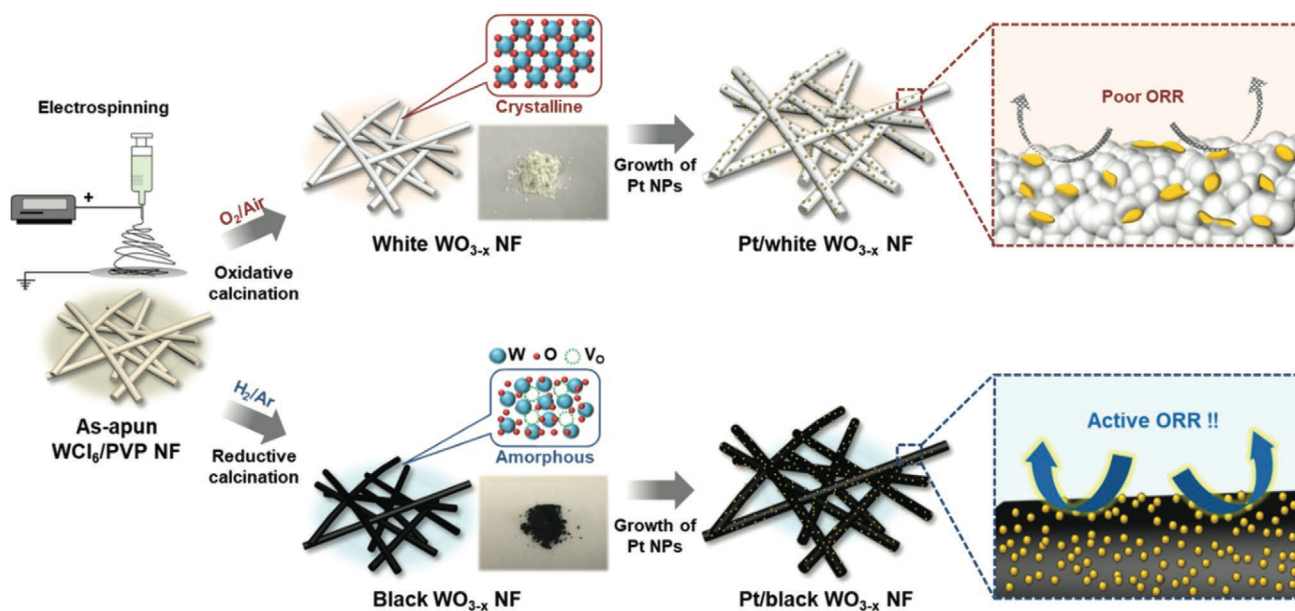
Figure 1. Schematic of the preparation procedures of Pt/white WO_{3-x} NFs and Pt/black WO_{3-x} NFs, their different morphologies, and the catalytic activities of these two materials in ORR.

(PVP) under a high magnetic field. The as-spun WCl_6/PVP composite fibers were collected with a ground substrate, and then heat-treated at 650 °C for 3 h under different conditions. Specifically, they were either subjected to oxidative calcination in O_2 or air or reductive calcination in a H_2/Ar atmosphere in a tube furnace. The first processing condition (oxidative calcination) led to white crystalline WO_3 or WO_{3-x} NFs, whereas the second one (reductive calcination) yielded poorly crystalline, amorphous, black WO_{3-x} NFs. The samples exhibited a clear difference in color (see the photographs of the white WO_{3-x} and black WO_{3-x} NF samples in Figure 1). Subsequently, the in situ formation and growth of Pt NPs as an ORR catalyst were achieved using a suspension containing a Pt precursor and NFs via the reduction of the Pt precursor with sodium borohydride. Finally, the Pt NP-loaded white WO_{3-x} and black WO_{3-x} NF samples were collected by filtration, and subjected to a two-step annealing process at 200 °C in air and H_2/Ar atmosphere (each lasted for 1 h). The structural and chemical properties of the obtained Pt/white WO_{3-x} and Pt/black WO_{3-x} NF samples were characterized by various techniques, and their ORR catalytic activities were evaluated.

Thermogravimetric analysis was first performed to analyze the pyrolysis behavior of the as-spun fibers of WCl_6 and PVP (Figure S1, Supporting Information). A gradual weight loss of ≈10% was observed between 30 and 300 °C, which is related to the evaporation of residual solvent and adsorbed species on the as-spun fibers.[16] Further, a drastic weight loss was observed between 300 and 400 °C, owing to the decomposition of the WCl_6 precursor. With a further increase in temperature, the pyrolysis of PVP occurred, followed by the removal of carbon and any organic residues; the process was completed at ≈600 °C.

The microstructural evolutions of the black WO_{3-x} NFs, white WO_{3-x} NFs and the fully oxidized white WO_3 NFs were studied by scanning electron microscopy (SEM) and transmission electron microscopy (TEM). **Figure 2**a,b shows the SEM images of the black WO_{3-x} NF samples obtained from the reductive calcination. The randomly entangled fibers with a very smooth surface were observed. The diameter of each fiber is in the range of 300–350 nm. For white WO_{3-x} NFs obtained from the calcination in air atmosphere, the overall nonwoven fiber structure similarly appeared in low-magnification SEM image (Figure 2c). However, a distinctive polycrystalline surface morphology of the fiber with the diameter of individual fibers being in the range of 285–290 nm, which is composed of densely packed grains of 50–100 nm size, is observed for white WO_{3-x} NFs (Figure 2d).[17] During the preparation of a fully oxidized white WO_3 NFs, we carried out the high-temperature calcination under O_2 atmosphere. As demonstrated in Figure 2e,f, severe grain growth of thermally sintered particles occurred. The overall thickness of the fiber reached ≈800 nm, which can lead to a reduction in the surface area for attaching the catalyst NPs. In the TEM images, no evident crystalline phases are observed for the black WO_{3-x} NFs (Figure 2g); instead, amorphous features are detected on the surface. As shown in the energy-dispersive X-ray spectroscopy (EDS) mapping image, W and O atoms are homogeneously distributed on the overall black WO_{3-x} NFs. On the other hand, a clear lattice fringe of 3.6 Å was observed in the white WO_{3-x} NFs; this spacing corresponds to the typical (200) plane

of the monoclinic WO_3 phase (Figure 2h). From the EDS mapping, WO_{3-x} NFs also have a uniform distribution of W and O in the bulk. The selected area electron diffraction (SAED) patterns of the two samples (Figure S2, Supporting Information) also support these observations; the SAED pattern of the white WO_{3-x} NFs shows clear dots related to the crystal planes, which formed a distinctive ring pattern, whereas the SAED pattern of the black WO_{3-x} NFs is a blurred image without any distinct rings.

X-ray diffraction (XRD) was performed for investigating the crystallographic structures of the white WO_{3-x} and black WO_{3-x} NF samples. The pattern of the white WO_{3-x} NFs (orange line; Figure S3, Supporting Information) could be indexed to the monoclinic WO_3 phase (JCPDS# 43–1035); it shows peaks corresponding to the (002), (020), and (200) planes of WO_3 at 23.24°, 23.7°, and 24.48°, respectively.[11c] In the XRD pattern of the black WO_{3-x} NFs (green line), a small peak related to the W_2C phase is observed at 42°, indicating that residual carbon is bound to the surrounding tungsten atoms. Although the overall pattern resembles that of WO_2 (JCPDS# 32–1393), disregarding the relative peak intensity, the whole gentle curve of the pattern indicates that the black WO_{3-x} NFs are largely composed of poorly crystalline or amorphous structural phases.

To investigate the chemical compositional changes of samples under different calcination conditions, we conducted the X-ray photoelectron spectroscopic (XPS) analysis of the pristine and surface-etched samples (white WO_3 NFs, white WO_{3-x} NFs, and black WO_{3-x} NFs).[18] We quantitatively characterized the degree of nonstoichiometry, which is correlated to the oxidation state of WO_{3-x}, using the following relationship[11c]

$$N = \frac{WO_3}{WO_{3-x}} \approx \frac{W^{6+}}{W^{4+} + W^{5+}} \tag{1}$$

where N is the numerical value of WO_3/WO_{3-x}, and W^{6+}, W^{5+}, and W^{4+} represent the contents of these species estimated from the deconvolution of the XPS profiles. The calculated N values for the white WO_3 NF, white WO_{3-x} NF, and black WO_{3-x} NF samples were 9.82, 9.68, and 2.22, respectively, indicating that the black WO_{3-x} NFs were off-stoichiometric to a higher degree, and thus, had a higher concentration of oxygen vacancies than the white WO_3 NFs and white WO_{3-x} NFs.

In the O 1s spectra (Figure 2j), the peaks at ≈530.4 eV (orange area) and ≈532.2 eV correspond to the lattice oxygen atoms and −OH species in the surface of pristine samples.[19a–c] The peaks at ≈533.5 eV are gradually increased from the white WO_3 NFs to black WO_{3-x} NFs, which is attributed to the reduced tungsten valence state, i.e., W^{4+} or W^{5+}. XPS analysis after surface etching is an effective way to observe the chemical composition of bulk materials. XPS spectra of the etched samples (Figure S4, Supporting Information) demonstrated significant spectral changes compared to those of the pristine states. Comparing white WO_3 NF to black WO_{3-x} NF, W^{5+}/W^{4+}-related peaks in both the W 4f and O 1s regions increase in the former, while the W^{6+} and lattice oxygen signals decrease. This means that the calcination atmosphere critically affects the crystalline structure of tungsten oxides, and the increased nonstoichiometric degree clearly appeared in the bulk materials. Specific compositions (especially O/W ratio) of the materials at
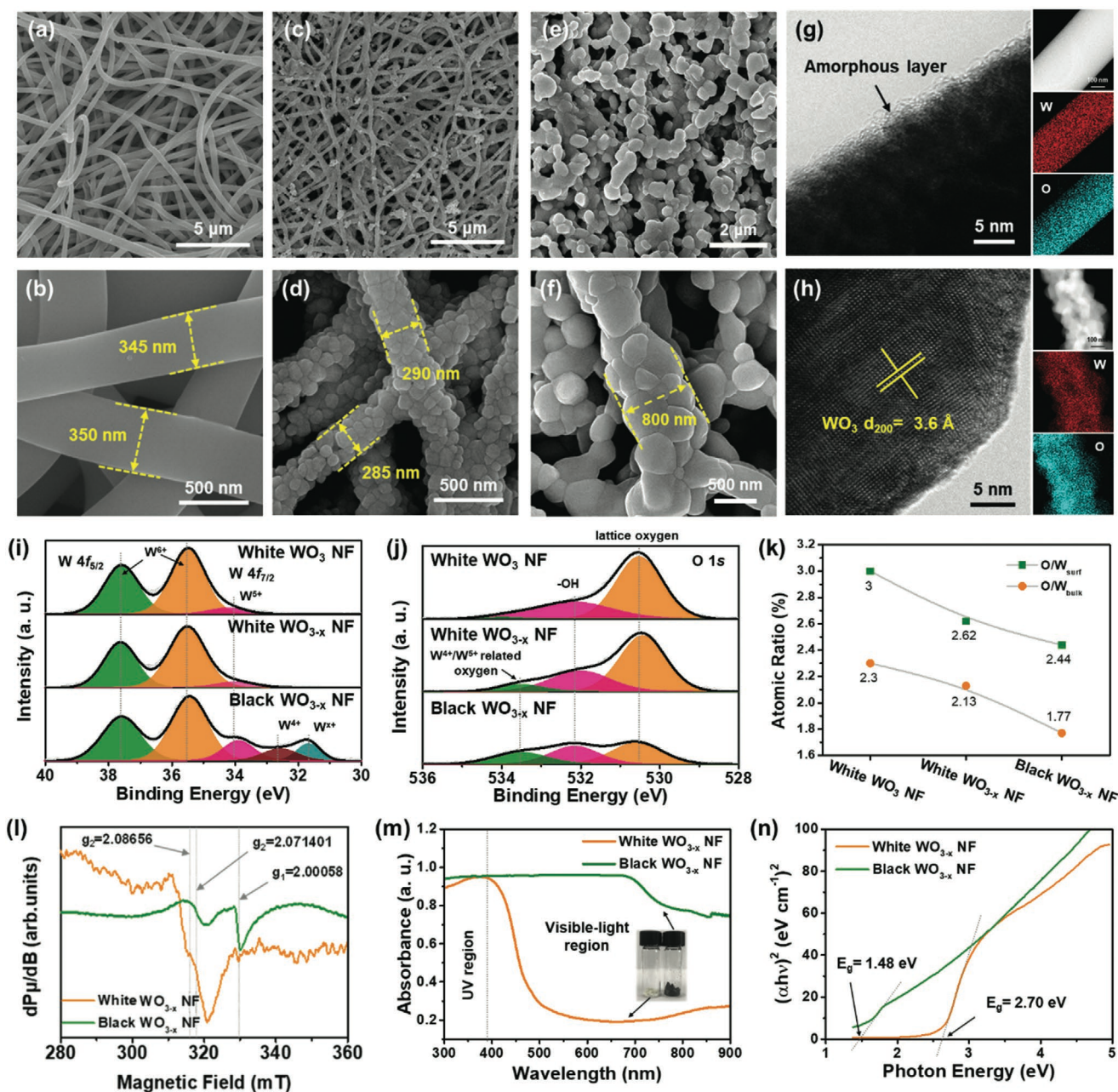
Figure 2. SEM images of a,b) black WO_{3-x} NFs, c,d) white WO_{3-x} NFs, and e,f) white WO_3 NFs (fully oxidized). TEM and EDS mapping images of g) white WO_{3-x} NFs and h) black WO_{3-x} NFs. XPS spectra in i) W 4f and j) O 1s regions of pristine white WO_3 NFs, white WO_{3-x} NFs, and black WO_{3-x} NFs. k) Atomic ratio of O to W at the surface and bulk regions (O/W$_{surf}$ and O/W$_{bulk}$, respectively) obtained from the XPS spectra of pristine and etched samples (white WO_3 NFs, white WO_{3-x} NFs, and black WO_{3-x} NFs). l) g-value of white WO_{3-x} NFs and black WO_{3-x} NFs estimated by ESR. m) UV–vis spectra of white WO_{3-x} NFs and black WO_{3-x} NFs (inset: digital photograph of white WO_{3-x} NFs and black WO_{3-x} NFs) and n) the corresponding Tauc plots.

the surface and bulk regions, obtained from the XPS spectra of the pristine and etched states, respectively, were also compared (Figure 2k). The atomic ratio O/W$_{surf}$ in the black WO_{3-x} NFs (2.44) is lower than that in the white WO_{3-x} NFs (2.62), as estimated based on the ratio between the total areas of the O 1s and W 4f XPS signals. The differences in oxygen deficiency are more evident in the bulk region, i.e., the O/W$_{bulk}$ ratios for white WO_3 NFs, white WO_{3-x} NFs, and black WO_{3-x} NFs are 2.3, 2.13, and 1.77, respectively. These data demonstrate that

the black WO_{3-x} NFs develop oxygen vacancies in the lattice during its post-treatment in a reductive environment, as shown below[10a]

$$2W^{6+/5} + O^{2-} + H_2 \rightarrow 2W^{5+/4+} + V_O + H_2O \qquad (2)$$
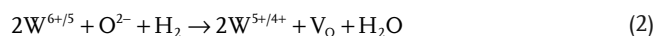
where O^{2-} denotes the lattice oxygen and V_O denotes the oxygen vacancy. We infer that the spontaneously formed oxygen-deficient surface under hydrogenation conditions accounts for the

amorphous surface of the black WO_{3-x} NF observed in the TEM images, instead of the stoichiometric crystalline WO_3 surface.

Electron spin resonance (ESR) spectroscopy was carried out to directly verify the existence of oxygen vacancies in the white WO_{3-x} NFs and black WO_{3-x} NFs (Figure 2l). In metal oxides, paramagnetic oxygen species generally exist both on the surface and in the bulk lattice. The values of g-tensors are derived from two different oxygen-related defects, such as the surface electron-trapping sites ($g_1 \cong 2.001$) of surface oxygen vacancies and lattice electron-trapping sites ($g_2 = 2.07$–2.08) in the bulk,[20] whereas the white WO_{3-x} NFs yielded only one peak at $g_2 = 2.07141$ for the lattice electron-trapping sites, the black WO_{3-x} NFs yielded two g-values, $g_2 = 2.08656$ and $g_1 = 2.00058$. The small differences in the g_2-values and peak intensities between the white and black samples indicate that O_2^- radicals are present in different surroundings in the two samples. Interestingly, the g_1-signal, corresponding to the free electrons located at the surface oxygen vacancies, was found only in the ESR spectrum of the black WO_{3-x} NFs, agreeing well with the XPS result.[11f] This proves that black WO_{3-x} has a relatively high abundance of surface oxygen vacancies than the white WO_{3-x} NFs, which affects its surface adsorption properties. We further conducted UV–vis spectroscopy to analyze the optical features of the white WO_{3-x} and black WO_{3-x} NF samples. In Figure 2m, the black WO_{3-x} NFs show much higher absorbance in the visible-light region (>380 nm) than the white WO_{3-x} NFs, which explains the stark color difference between the two samples (inset). The optical bandgap values were calculated using the Tauc equation; as shown in Figure 2n, the black WO_{3-x} NFs have a bandgap of 1.48 eV, which is much lower than that of the white WO_{3-x} NFs (2.7 eV). These results imply that the unique oxygen-deficient, less crystalline, black WO_{3-x} NFs with a reduced bandgap can have better surface adsorption properties and electrical conductivity than the relatively more crystalline white WO_{3-x} NFs.

The surface oxygen vacancies (V_O) in metal oxides are critical for promoting the electrocatalytic activity of the supported noble metal catalysts, such as Pt, Pd, or Au, because they influence the adhesion between the support and metal species and also affect the electronic structure of the metal.[21] To clarify the morphological and chemical differences in the Pt-loading behaviors of the white WO_{3-x} NFs and black WO_{3-x} NFs as catalyst supports, we conducted TEM, EDS, and XPS analyses after loading Pt. Figure 3a–c shows the TEM images of the Pt-loaded white WO_{3-x} NFs (Pt/white WO_{3-x} NFs) at different magnifications. The polycrystalline WO_3 structure was preserved after Pt loading. As shown in the high-resolution image, Pt particles appeared as black dots on the surface of the WO_3 NFs; these are
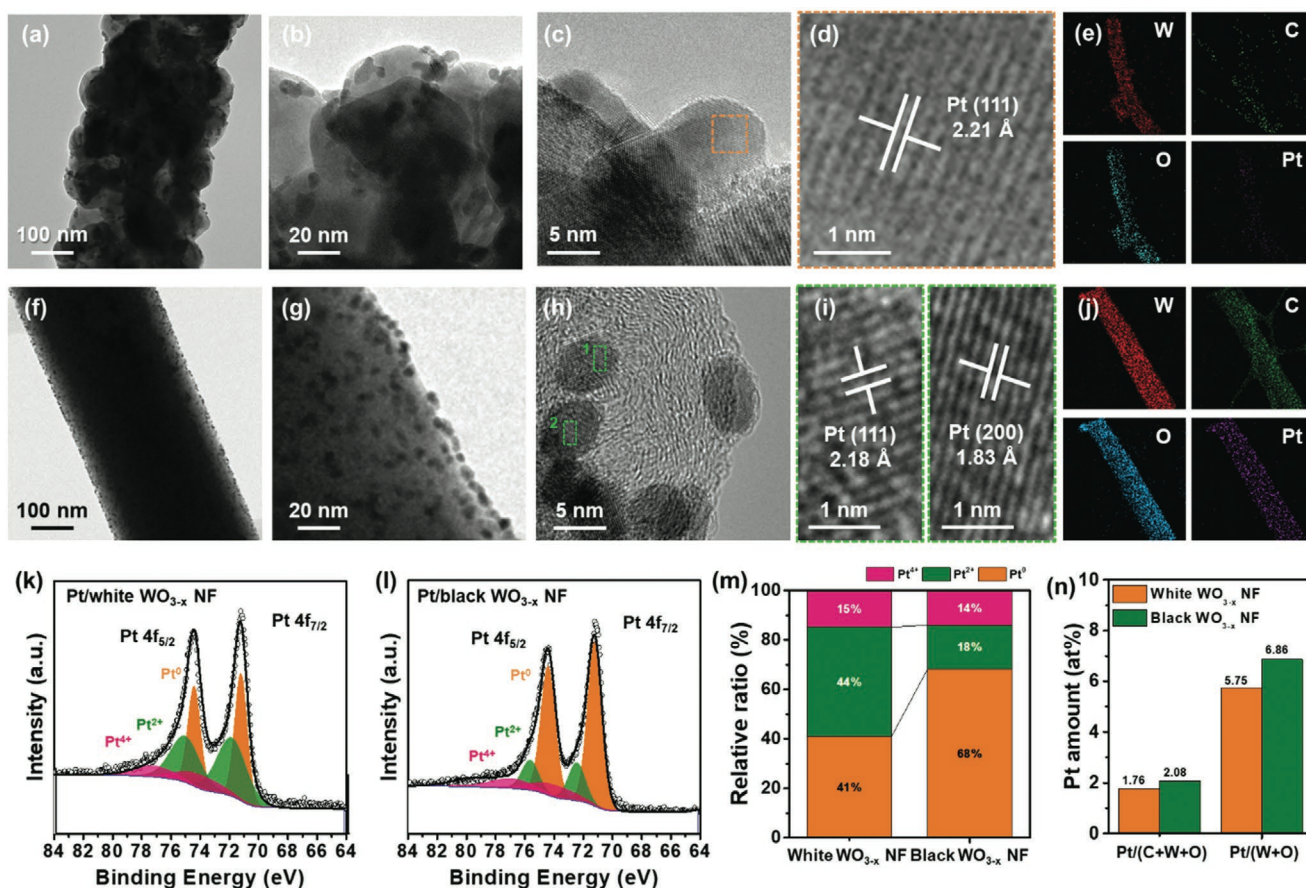
Figure 3. a–d) TEM images at different magnifications and e) EDS mapping images of Pt/white WO_{3-x} NFs. f–i) TEM images at different magnifications and j) EDS mapping images of Pt/black WO_{3-x} NFs. XPS Pt 4f profiles of k) Pt/white WO_{3-x} NFs and l) Pt/black WO_{3-x} NFs. m) Relative ratios of different Pt species based on the area of XPS Pt 4f profiles, and n) amounts of Pt loaded on Pt/white WO_{3-x} NFs and Pt/black WO_{3-x} NFs.

marked with dashed orange circles (Figure 3b). Further, some aggregates in the lateral direction were also observed. The particles have an average diameter of 10.67 nm and show a lattice fringe spacing of 2.21 Å,[22] which corresponds to the (111) plane of Pt (see Figure 3d). The EDS mapping image confirmed that the W, O, C, and Pt atoms were homogeneously distributed in the overall fiber structure (Figure 3c).

For the Pt/black WO_{3-x} NFs, the TEM images showed a large number of small dark dots distributed on the smooth surface of the NFs at a high density (Figure 3g,h), implying that the surface of the black WO_{3-x} NFs consists of numerous nucleation sites for adsorbing the Pt precursor. Furthermore, the average size of the Pt NPs is less than 5 nm, which is much smaller than that of the Pt NPs (10–20 nm) loaded on white WO_{3-x} NFs. The lattice fringes of the Pt NPs are spaced 2.18 and 1.83 Å apart, and they correspond to the (111) and (200) planes of metallic Pt, respectively (Figure 3i). As shown in Figure 3j, W, O, C, and Pt signals were detected uniformly on the fiber structure, but a much higher Pt signal (purple) was detected for the Pt/black WO_{3-x} NFs than for the Pt/white WO_{3-x} NFs (Figure 3j). Interestingly, the intensities of the XPS shoulder peaks related to W^{5+} and W^{4+} at 33.3 and 32.3 eV, respectively, evidently decreased after Pt loading (Figure S5, Supporting Information). This implies that the Pt NPs are attached selectively to the oxygen vacancy sites, and the unsaturated oxidation states of W^{x+} ($x < 6$) are compensated by the attached Pt NPs.

Furthermore, it has been reported that the electronic structure and chemical states of catalytic NPs are significantly affected by the supporting material.[2c,12a] For example, a shift in the binding energy of the surface Pt NPs or a change in the oxidation state of the Pt NPs was observed when they were supported on different supporting materials. To verify the effect of the support on the properties of the Pt NPs, we conducted XPS analysis of the Pt NPs in Pt/white WO_{3-x} NFs and Pt/black WO_{3-x} NFs. As shown in Figure 3k,l, the Pt 4f spectra could be deconvoluted into the Pt $4f_{7/2}$ and Pt $4f_{5/2}$ peaks of the Pt^0, Pt^{2+}, and Pt^{4+} species. The binding energies and relative amounts of the species (Pt^0, Pt^{2+}, and Pt^{4+}) determined from the deconvoluted peaks are summarized in **Table 1**. For the Pt NPs loaded on the white WO_{3-x} NFs, the relative amounts of Pt^0, Pt^{2+}, and Pt^{4+} were determined to be 40.9%, 44.3%, and 14.8%, respectively (Figure 3m). On the other hand, Pt^0 was predominantly detected on the black WO_{3-x} NFs, and the proportions of the Pt species were determined to be Pt^0 (68%), Pt^{2+}(18%), and Pt^{4+}(14%). This result indicates that more metallic Pt was
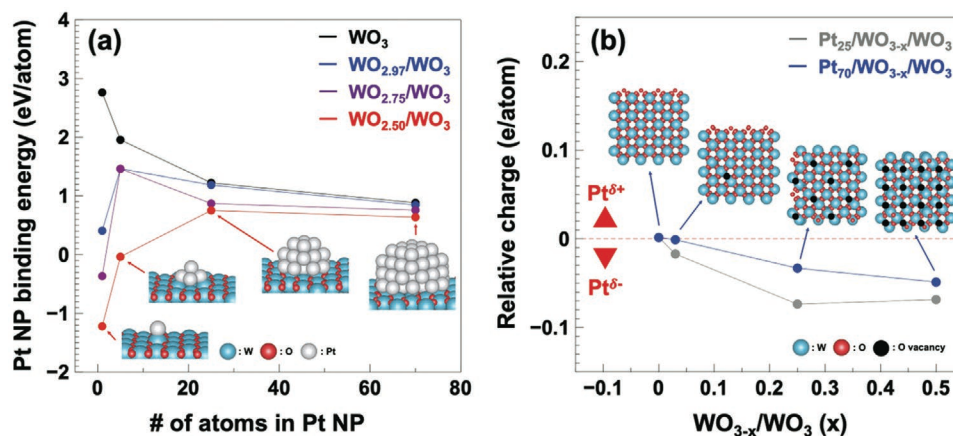
formed on the black WO_{3-x} NFs than on the white WO_{3-x} NFs, although the same Pt-loading process was used for both the samples. We further compared the amount of Pt loaded on the two types of NFs by comparing the Pt atomic ratio with the sum of "C+O+W" and "O+W" estimated from the peak areas of various species in the XPS profiles (Figure 3n). A higher number of Pt NPs were found on the black WO_{3-x} NFs than on the white WO_{3-x} NFs. Based on the overall analysis, we conclude that the supporting material indeed affects the growth behavior of the supported metal NPs, as confirmed by the number and size of the loaded Pt NPs as well as their chemical states.

To further validate the experimental findings of the Pt loading on the white WO_{3-x} and black WO_{3-x} NFs, we performed density functional theory (DFT) calculations using Pt NPs of different sizes and binding energies loaded on WO_{3-x} NFs with different numbers of oxygen vacancies.[8,23] We modeled the WO_3 (001) surface structure (Figure S6a, Supporting Information) based on the XRD results discussed earlier, and also considered different numbers of oxygen vacancies to simulate the structure of the WO_{3-x} NFs (Figure S6b–d, Supporting Information) using structures such as WO_3, $WO_{2.97}/WO_3$ (1 oxygen vacancy), $WO_{2.75}/WO_3$ (8 oxygen vacancies), and $WO_{2.50}/WO_3$ (16 oxygen vacancies). Pt clusters of four different sizes, consisting of 1, 5, 25, and 70 atoms (Figure S6e–h, Supporting Information), were attached to the WO_{3-x} surface, as shown in **Figure 4**a. The binding energies of Pt species in the Pt NPs increased with the number of oxygen vacancies, regardless of their size; however, a very interesting trend was observed in the change of the binding energy of the Pt NPs of different sizes. The Pt binding energy on WO_3 enhanced, as the size of the Pt NP increased, but $WO_{2.50}/WO_3$ showed an opposite trend, implying that smaller Pt NPs are more stable than larger ones on $WO_{2.50}/WO_3$. In other words, small Pt NPs supported on WO_3 grew in size owing to the diffusion process, but this process was not favored in the case of $WO_{2.50}/WO_3$ because of the low stability of large Pt NPs. Thus, we can infer that the suppressed growth of the supported Pt NPs is a result of the oxygen deficiency of the black WO_{3-x} NFs (or $WO_{2.50}/WO_3$) based on the results of our calculation, which is consistent with the TEM analysis presented in Figure 3.

We also performed Bader charge analyses to verify the valence charge difference at the supported Pt NPs (Pt_{25} and Pt_{70}) to confirm the results of XPS analysis in Figure 3k,l.[24] The relative charge presented in Figure 4b was calculated by subtracting the average valence charge of Pt metal from that of

Table 1. Binding energies and relative integrated areas from XPS Pt 4f profiles of Pt/white WO_{3-x} NFs and Pt/black WO_{3-x} NFs in the initial state and after ADT for 2000 cycles.

Sample	Species	Initial state		After 2000 cycles	
		Binding energy [eV]	Relative area [%]	Binding energy [eV]	Relative area [%]
Pt/white WO_{3-x} NFs	Pt^0	71.21, 74.41	40.9	71.40, 74.60	34.0
	Pt^{2+}	71.80, 75.00	44.3	71.71, 74.91	42.1
	Pt^{4+}	74.00, 77.20	14.8	74.00, 77.20	22.9
Pt/black WO_{3-x} NFs	Pt^0	71.22, 74.42	68.2	71.16, 74.36	38.3
	Pt^{2+}	72.40, 75.60	17.8	71.80, 75.00	42.2
	Pt^{4+}	74.00, 76.90	14.0	74.00, 77.20	19.5

**ADVANCED
SCIENCE NEWS**

www.advancedsciencenews.com

NANO · MICRO
small

www.small-journal.com

Figure 4. a) Binding energies of Pt NPs of different sizes supported on WO_{3-x} NFs and b) average charge difference between the supported Pt NPs and Pt metal, where negative values indicate the reduction of the supported Pt NPs.
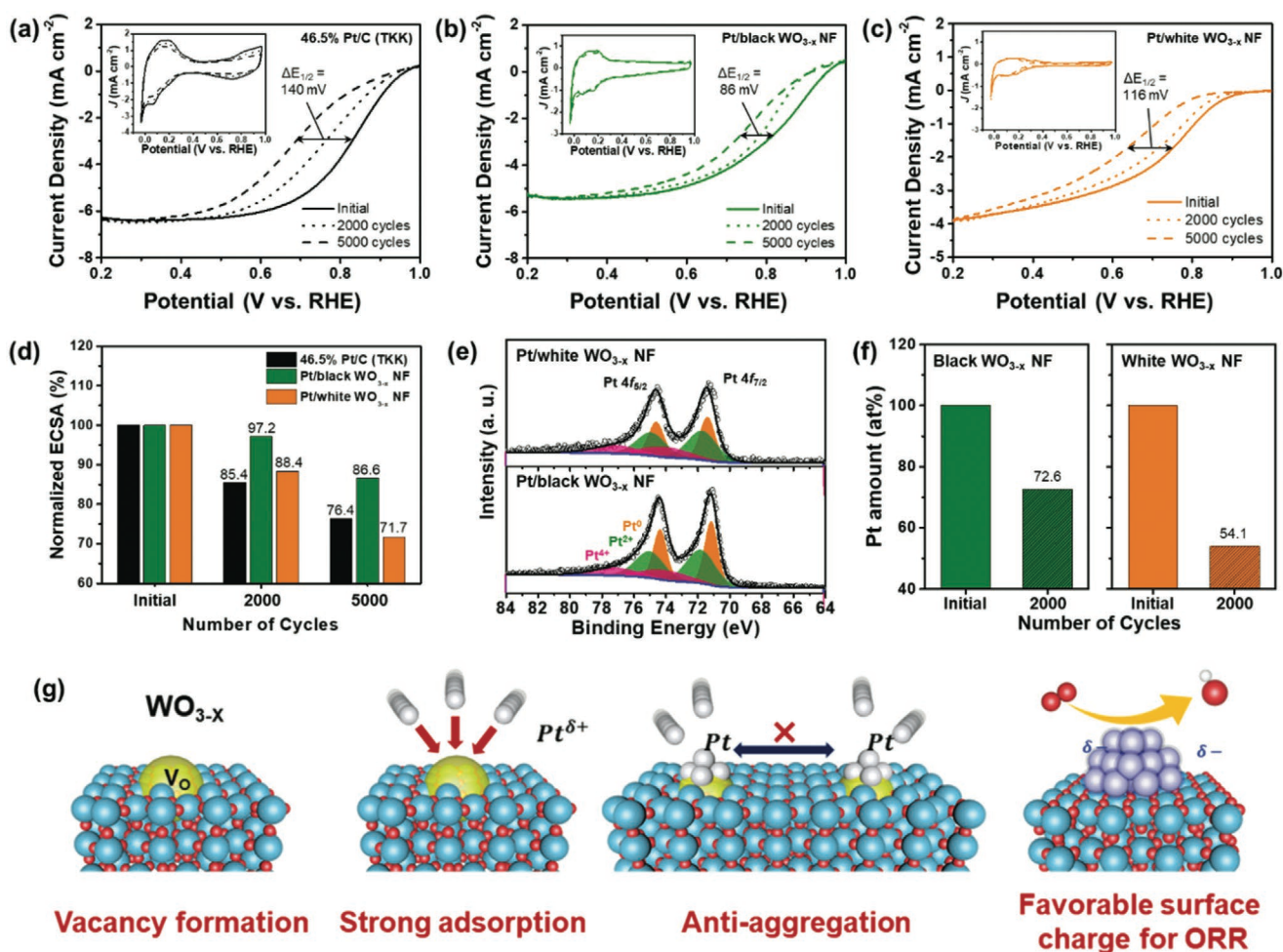
the supported Pt NP; therefore, the positive and negative signs represent oxidized ($Pt^{\delta+}$) and reduced ($Pt^{\delta-}$) Pt NPs, respectively. As clearly shown in Figure 4b, the supported Pt NP is slightly oxidized on the stoichiometric WO_3 surface regardless of its size, but it is reduced as the number of oxygen vacancies is increased. That is, the number of oxidized Pt atoms decreases systematically with increasing oxygen vacancies. In our previous study, we have observed that the oxygen deficiency could reduce Au NPs loaded on TiO_{2-x}.[25] We believe that the oxygen vacancies aid the reduction of the supported Pt NP as wells as WO_{3-x} by releasing electrons held by the oxygen species. Thus, based on DFT calculations, we successfully confirmed the experimental findings in terms of the binding energy and relative charge of the supported Pt NPs. We found that Pt NPs on the white WO_{3-x} NFs could grow easily, while their growth is not facile on the black WO_{3-x} NFs because of the unfavorable energetics. Furthermore, the reduced Pt NP charge state on the black WO_{3-x} NFs was also confirmed.

To verify the electrochemical properties of the developed supports, we evaluated the ORR performances of the prepared samples and compared them with those of a commercial Pt/C (TKK) via half-cell measurements in 0.1 M $HClO_4$. Figure S7 (Supporting Information) illustrates the ORR polarization curves of the Pt/white WO_3 NFs, Pt/white WO_{3-x}, Pt/black WO_{3-x} NFs, and Pt/C in an O_2-saturated electrolyte. All the linear sweep voltammetry (LSV) curves were recorded at a scan rate of 5 mV s^{-1} and 1600 rpm. Interestingly, the ORR activity of Pt NPs improves in terms of both limiting current density and half-wave potentials as the oxygen deficiencies of the supports increase. Even though the limiting current of Pt/black WO_{3-x} NFs was lower than that of Pt/C, the half-wave potential of Pt/black WO_{3-x} NFs was similar to that of Pt/C ($E_{1/2}$ = 0.85 V). The ORR catalytic efficiency of the Pt NPs was also determined from the charge-transfer number. Figure S8 (Supporting Information) shows the LSV curves at different rotating speeds (625, 900, 1225, 1600, and 2025 rpm) of Pt/C, Pt/black WO_{3-x} NFs, and Pt/white WO_{3-x} NFs, and corresponding Koutecky–Levich (K–L) plots at different potentials. According to the slopes of K–L plots, the number of transferred electrons (n) of the Pt/black WO_{3-x} NF electrode was calculated to be 3.6, indicating

that primarily a four-electron ORR process occurred on Pt supported on the black WO_{3-x} NFs.[26] The calculated n value of the Pt/white WO_{3-x} NFs is only 3.2, indicating an inferior ORR catalytic activity. The enhanced current density and ORR activity of the black WO_{3-x} NF sample can be explained by the following two properties of the support material: it has sufficient electrical conductivity for activating the supported catalyst and the active surface area of the Pt catalyst loaded on it is high, which is consistent with the TEM observations.

The most crucial role of the catalyst supports is maintaining the catalytic activity of the supported catalysts. Usually, the accelerated durability test (ADT), by repeating the fast cyclic voltammetry (CV) scans, is adopted to investigate the stability and durability of the catalyst–support system. Therefore, we conducted ADTs with Pt/white WO_{3-x} NFs, Pt/black WO_{3-x} NFs, and commercial Pt/C, and compared the initial LSV and CV curves with those after 2000 and 5000 cycles. As depicted in **Figure 5**a, the LSV curves change significantly with the number of cycles. The half-wave potential changes significantly ($\Delta E_{1/2}$ = 140 mV) after 5000 ADT cycles. This behavior generally occurs in the carbon-supported Pt NPs because of severe carbon corrosion and the reduction of active Pt NPs during CV,[2c,12d] which is also confirmed by the reduction in the area of the CV curves after cycling. Interestingly, the Pt/black WO_{3-x} NF electrode maintains its original performance after 5000 ADT cycles with a small displacement of the $E_{1/2}$ position ($\Delta E_{1/2} \cong 86$ mV) and almost no changes in the CV curves (Figure 5b). The Pt/white WO_{3-x} NFs demonstrate inferior performance, with a $\Delta E_{1/2}$ of ≈116 mV after 5000 ADT cycles (Figure 5c). Figure 5d depicts the changes in the normalized electrochemical surface area (ECSA) after the ADT cycles. As expected, Pt/black WO_{3-x} NFs have the highest maintenance, with an initial ECSA value of 86.6% after 5000 cycles. At the same time, commercial Pt/C and Pt/white WO_{3-x} demonstrate significant degradation of ECSA, that is, a reduction to 76.4% and 71.7%, respectively, after the ADT cycles. Even though the noncorrosive WO_{3-x} NFs were adopted as the support materials, the electrochemical durability was largely dependent on the oxygen deficiency.

In order to figure out the chemical interaction between Pt NPs and surface states of oxygen defective WO_{3-x} NFs, we

**ADVANCED
SCIENCE NEWS**

www.advancedsciencenews.com

**NANO · MICRO
small**

www.small-journal.com

Figure 5. LSV and CV curves (insets) of a) commercial Pt/C (TKK), b) Pt/black WO_{3-x} NFs, and c) Pt/white WO_{3-x} NFs in 0.1 M $HClO_4$, initial curves and those after 2000 and 5000 ADT cycles are presented. d) Normalized ECSA changes of Pt/C, Pt/black WO_{3-x} NFs, and Pt/white WO_{3-x} NFs after 2000 and 5000 ADT cycles. e) XPS Pt 4f profiles. f) The changes in Pt amounts loaded on black WO_{3-x} NFs and white WO_{3-x} NF after 2000 ADT cycles. g) Proposed mechanism for the improved ORR activity of Pt/black WO_{3-x} NF.

further investigated the ex situ XPS analysis with Pt/white WO_{3-x} NFs and Pt/black WO_{3-x} NFs after 2000 ADT cycles. After the ADT cycles, the Pt^{2+} peaks were dominant for both the samples (Figure 5c and Table 1), but a stronger Pt^0 peak was observed for the Pt/black WO_{3-x} NFs (38.3%) than for the Pt/white WO_{3-x} NFs (34.0%). Moreover, the Pt/white WO_{3-x} NF and Pt/black WO_{3-x} NF samples showed W^{5+} peaks at ≈34.2 eV, which became noticeable after the cycling test, presumably owing to the electrochemical reduction of the support material (Figure S9, Supporting Information). The lower binding energy peak at ≈32.4 eV is attributed to W^{4+} in the black WO_{3-x} NFs, indicating that its surface oxygen deficiency was maintained after the cycling test. The direct evidence of the enhanced durability of the Pt/black WO_{3-x} NFs was obtained from the amount and size of the Pt NPs remaining on the support surface after the ADT. As shown in Figure 5f, the atomic percentage of Pt remaining on the white WO_{3-x} NFs decreased by 54.1% (4.97 → 3.11 in atomic percent) as compared to that in its initial state, while 72.58% of Pt was preserved on the black WO_{3-x} NFs (decrease: 6.86 → 4.97 in atomic percent). The enlarged Pt NPs

on the white WO_{3-x} NFs indicate significant aggregation after the ADT (Figure S10, Supporting Information). In contrast, the small Pt NPs were still locally positioned on the surface of the black WO_{3-x} NFs. We speculate that the strong adsorption of the Pt NPs on the oxygen-deficient surface of the NFs favorably preserves the original Pt NP morphology and catalytic activity even after the ADT. In summary, the outstanding durability of the Pt/black WO_{3-x} NFs was confirmed by comparing the chemical state of Pt NPs, residual amount of Pt remaining on the surface, and morphological differences in the supported Pt NPs. Figure 5g presents the proposed mechanism for the enhanced catalytic activity and stability of the Pt/black WO_{3-x} NFs. Surface oxygen vacancies were intentionally formed on the black WO_{3-x} NFs via the reductive calcination of the precursor. The oxygen vacancy acted as a predominant anchoring site for Pt^{4+} ions, while the adjacent surface was energetically unfavorable for the lateral growth of the Pt particles, resulting in nonaggregated discrete Pt NPs at the vacancy sites. These Pt NPs exhibit a more metallic and negatively charged surface, leading to high ORR catalytic activity and stability compared

to those of the Pt NPs loaded on the crystalline surface of the white WO_{3-x} NFs.

3. Conclusions

In summary, we prepared oxygen-deficient WO_{3-x} NFs with low metal valence by electrospinning the W precursor and then conducting reductive calcination of the electrospun fibers. The amorphous black WO_{3-x} NFs have sufficient electrical conductivity owing to their reduced bandgap, while the oxygen-deficient surface modulates the surface-adsorption properties, providing numerous vacancy sites for anchoring the Pt precursor, which is energetically favorable for forming a large number of small Pt NPs. The obtained Pt/black WO_{3-x} NFs exhibited better catalytic activity and stability in ORR in acidic media as compared to those of Pt/white crystalline WO_{3-x} NFs. The results of this study indicate that a simple modification of the material processing, such as the calcination condition, can improve the properties of metal oxides for electrochemical applications. In this study, we obtained oxygen-deficient tungsten oxide as a robust support for Pt, which can be applied in electrochemical ORR. We believe that this work will inspire the design of hybrid metal/metal oxide hybrid catalyst–support systems, leading to efficient and long-lasting ORR-based devices such as fuel cells and air-breathing batteries.

4. Experimental Section

Materials: WCl_6 (99.9%), PVP (M_w = 1300 000), dimethylformamide (DMF, anhydrous, 99.8%), acetic acid (CH_3COOH, 99.9%), hexachloroplatinic acid hexahydrate ($H_2PtCl_6 \cdot 6H_2O$, 37.50% Pt basis), sodium borohydride ($NaBH_4$, powder, >98.0%), anhydrous sodium acetate (CH_3COONa, >99%), and ethanol (C_2H_5OH, 99.8%) were purchased from Sigma–Aldrich. All materials were used as received without further purification.

Synthesis of White WO_3 NFs, White WO_{3-x} NFs, and Black WO_{3-x} NFs: First, a mixture of WCl_6 (1.5 g), CH_3COOH (0.2 g), and PVP (1.25 g) was dissolved in DMF (10 g), and the obtained solution was stirred magnetically using a stir bar (500 rpm) for 10 h at 25 °C. Then, the solution was transferred to a 10 mL Luer lock syringe. The syringe was mounted on a syringe pump, and the solution was injected through a 21 gauge needle under an electrical field generated by applying a voltage of 15 kV, and the fibers were collected with a ground substrate. The feeding rate in the electrospinning process was set to 0.8 µL min^{-1}, and the distance between the needle and cylindrical collector was ≈15 cm. After electrospinning, the as-spun fibers were preheated at 300 °C for 1 h (10 °C min^{-1}) in air. Subsequently, the preheated fibers were further annealed at 650 °C for 3 h under O_2, air, and H_2/Ar (5%/95%, v/v) atmospheres to obtain white WO_3 NFs, white WO_{3-x} NFs, and black WO_{3-x} NFs, respectively.

Loading of Pt NPs on White WO_3 NF, White WO_{3-x} NF, and Black WO_{3-x} NF Samples: The white WO_3 NFs, white WO_{3-x} NFs, or black WO_{3-x} NFs (50 mg) were dispersed in EtOH (100 mL) and sonicated for 1 h. Then, $H_2PtCl_6 \cdot 6H_2O$ (108 mg) and CH_3COONa (172 mg) were dissolved separately in EtOH (20 mL each), and the two solutions were added simultaneously to the NF suspension. The resulting mixture was sonicated for 1 h. Then, a solution of $NaBH_4$ (0.16 g) in (EtOH (20 mL) was added dropwise to the above mixture and allowed to react for 60 min to form Pt NPs. After that, the mixture was filtered and the precipitate was washed several times with EtOH and deionized (DI) water. The collected samples (Pt NP-loaded white WO_3 NFs, white WO_{3-x} NFs, and black WO_{3-x} NFs) were first annealed at 200 °C for 1 h in air and subsequently at 200 °C for 1 h under H_2/Ar (5%/95% v/v).

Material Characterization: The surface and cross-sectional morphologies of the samples were observed by SEM (S-4300SE by Hitachi)

and TEM (JEM-2100F, Cs corrector by JEOL/CEOS). The crystalline or amorphous structure of the samples was analyzed by XRD (Ultima IV by Rigaku). The oxidation states of the surface elements were determined by XPS (K-alpha, Thermo UK). ESR experiments were conducted using an X-band spectrometer (JES-FA100, JEOL, USA) at 100 kHz modulation frequency using a power of 0.998 mW at −100 °C. UV–vis absorption spectra were recorded on a Lambda 1050 (Perkin Elmer) spectrometer equipped with a Labsphere diffuse reflectance accessory.

Electrochemical Characterization: Electrochemical tests were conducted using a three-electrode system using a glassy carbon electrode (GCE; 3 mm diameter) loaded with the catalyst (Pt-loaded white WO_3 NFs, WO_{3-x} NFs, or black WO_{3-x} NFs) as the working electrode, Pt coil as the counter electrode, and an Ag/AgCl electrode (filled with 3 м NaCl) as the reference electrode. To prepare the working electrode, the catalyst (4 mg) and a Nafion perfluorinated resin solution (80 µL; 5 wt% in a mixture of lower aliphatic alcohols and 15–20% water) were added to a water/isopropyl alcohol mixture (3:1 v/v; 1 mL) and sonicated for 30 min to form a catalyst ink. Then, the homogeneously mixed catalyst ink (14 µL) was pipetted onto the GCE (0.285 mg cm^{-2}) and then the GCE was dried overnight on a hot plate at 60 °C. Cyclic voltammetry was conducted in a N_2-saturated 0.1 м $HClO_4$ solution at a scan rate of 5 mV s^{-1}. Linear scan voltammetry was conducted to evaluate the ORR activities of the catalysts at a scan rate of 5 mV s^{-1}. The electrode was rotated at 1600 rpm in a 0.1 м $HClO_4$ solution. All potentials measured with respect to Ag/AgCl in the electrochemical analyses were converted to the standard hydrogen potential using the hydrogen electrode calibration method, $E_{RHE} = E_{Ag/AgCl} + 0.267$ V, and the details are given in Figure S11 (Supporting Information).

Ex Situ Characterization of the Samples: To confirm the surface morphology and composition ex situ, both the Pt/white WO_{3-x} NF and Pt/black WO_{3-x} NF catalysts were characterized by high-resolution transmission electron microscopy (HRTEM) and XPS after 2000 cycles of ADT in the voltage window of 0.6–1.1 V (vs reversible hydrogen electrode (RHE)) in a 0.1 м $HClO_4$ solution at a scan rate of 10 mV s^{-1}.

Computational Study: Generalized gradient approximation-level, spin-polarized DFT calculations were performed using the Vienna ab initio simulation package (VASP) using a plane-wave basis set with a cut-off energy of 400 eV. The Perdew–Burke–Ernzerhof (PBE) functional was used to describe electron exchange and correlation.[27] The Brillouin zone was sampled at the gamma point, which was found to be sufficient given the large system size. The convergence criteria for the electronic and geometric optimizations were 10^{-5} eV and 10^{-2} eV Å^{-1}, respectively. The WO_{3-x} (001) slab was modeled with a tetragonal structure (space group: *P4/ncc*)[28] with different numbers of oxygen vacancies, including perfect WO_3, and expanded to a 4 × 4 × 1 supercell to support Pt NPs of different sizes on the surface. The stoichiometric (or white) WO_{3-x} and oxygen-deficient (or black) WO_{3-x} surface slabs had a 20 Å vacuum gap in the z-direction; the bottom single WO_3 layer was fixed in its bulk-state position, and the other layers were fully relaxed during the calculations. The following simple equation was used to calculate the binding energy (ΔE_{BE}) of Pt clusters on different WO_{3-x} systems[28b]

$$\Delta E_{BE} = (\Delta E_{slab+Pt} - \Delta E_{slab} - n * \Delta E_{Pt})/n \tag{3}$$

where $\Delta E_{slab+Pt}$ is the total energy after the binding of Pt NPs, ΔE_{slab} is the total energy of the WO_{3-x} surface, ΔE_{Pt} is the energy of bulk Pt per atom, and n is the number of atoms in the Pt NP.

Supporting Information

Supporting Information is available from the Wiley Online Library or from the author.

Conflict of Interest

The authors declare no conflict of interest.

Data Availability Statement

Research data are not shared.

Keywords

catalyst supports, electrospinning, nanofibers, ORR, oxygen deficiency, WO$_3$

[1] a) J.-W. Jung, G.-Y. Kim, N.-W. Lee, W.-H. Ryu, *Appl. Surf. Sci.* **2020**, *533*, 147496; b) N.-W. Lee, J.-W. Jung, J.-S. Lee, H.-Y. Jang, I.-D. Kim, W.-H. Ryu, *Electrochim. Acta* **2018**, *263*, 417; c) N.-W. Lee, K. R. Yoon, J.-Y. Lee, Y. Park, S.-J. Pyo, G.-Y. Kim, D.-H. Ha, W.-H. Ryu, *ACS Appl. Energy Mater.* **2019**, *2*, 3513.

[2] a) O. Lori, L. Elbaz, *Catalysts* **2015**, *5*, 1445; b) H. Lv, S. Mu, *Nanoscale* **2014**, *6*, 5063; c) J. M. Kim, Y. J. Lee, S.-h. Kim, K.-H. Chae, K. R. Yoon, K. A. Lee, A. Byeon, Y. S. Kang, H.-Y. Park, M. K. Cho, H. C. Ham, J. Y. Kim, *Nano Energy* **2019**, *65*, 104008.

[3] a) L. Du, Y. Shao, J. Sun, G. Yin, J. Liu, Y. Wang, *Nano Energy* **2016**, *29*, 314; b) R. Borup, J. Meyers, B. Pivovar, Y. S. Kim, R. Mukundan, N. Garland, D. Myers, M. Wilson, F. Garzon, D. Wood, P. Zelenay, K. More, K. Stroh, T. Zawodzinski, J. Boncella, J. E. McGrath, M. Inaba, K. Miyatake, M. Hori, K. Ota, Z. Ogumi, S. Miyata, A. Nishikata, Z. Siroma, Y. Uchimoto, K. Yasuda, K. Kimijima, N. Iwashita, *Chem. Rev.* **2007**, *107*, 3904.

[4] a) S. Y. Huang, P. Ganesan, S. Park, B. N. Popov, *J. Am. Chem. Soc.* **2009**, *131*, 13898; b) G. Wu, M. A. Nelson, N. H. Mack, S. Ma, P. Sekhar, F. H. Garzon, P. Zelenay, *Chem. Commun.* **2010**, *46*, 7489; c) Z.-Z. Jiang, Z.-B. Wang, Y.-Y. Chu, D.-M. Gu, G.-P. Yin, *Energy Environ. Sci.* **2011**, *4*, 728.

[5] a) T. Masuda, H. Fukumitsu, K. Fugane, H. Togasaki, D. Matsumura, K. Tamura, Y. Nishihata, H. Yoshikawa, K. Kobayashi, T. Mori, K. Uosaki, *J. Phys. Chem. C* **2012**, *116*, 10098; b) Y. Y. Chu, Z. B. Wang, Z. Z. Jiang, D. M. Gu, G. P. Yin, *Adv. Mater.* **2011**, *23*, 3100.

[6] K. Sasaki, L. Zhang, R. R. Adzic, *Phys. Chem. Chem. Phys.* **2008**, *10*, 159.

[7] P. A. Shinde, S. C. Jun, *ChemSusChem* **2020**, *13*, 11.

[8] K. R. Yoon, J. M. Kim, K. A. Lee, C.-K. Hwang, S. G. Akpe, Y. J. Lee, J. P. Singh, K. H. Chae, S. S. Jang, H. C. Ham, J. Y. Kim, *J. Power Sources* **2021**, *496*, 229798.

[9] a) Y. Lu, Y. Jiang, X. Gao, X. Wang, W. Chen, *J. Am. Chem. Soc.* **2014**, *136*, 11687; b) M. S. Saha, M. N. Banis, Y. Zhang, R. Li, X. Sun, M. Cai, F. T. Wagner, *J. Power Sources* **2009**, *192*, 330.

[10] a) J. Song, Z.-F. Huang, L. Pan, J.-J. Zou, X. Zhang, L. Wang, *ACS Catal.* **2015**, *5*, 6594; b) H. Yu, F. Chen, X. Li, H. Huang, Q. Zhang, S. Su, K. Wang, E. Mao, B. Mei, G. Mul, T. Ma, Y. Zhang, *Nat. Commun.* **2021**, *12*, 4594; c) H. Yu, J. Li, Y. Zhang, S. Yang, K. Han, F. Dong, T. Ma, H. Huang, *Angew. Chem., Int. Ed. Engl.* **2019**, *58*,

3880; d) F. Chen, Z. Ma, L. Ye, T. Ma, T. Zhang, Y. Zhang, H. Huang, *Adv. Mater.* **2020**, *32*, 1908350.

[11] a) S. J. Choi, I. Lee, B. H. Jang, D. Y. Youn, W. H. Ryu, C. O. Park, I. D. Kim, *Anal. Chem.* **2013**, *85*, 1792; b) J. Qin, M. Cao, N. Li, C. Hu, *J. Mater. Chem.* **2011**, *21*, 17167; c) P. Chen, M. Baldwin, P. R. Bandaru, *J. Mater. Chem. A* **2017**, *5*, 14898; d) H. Xu, J. Gao, M. Li, Y. Zhao, M. Zhang, T. Zhao, L. Wang, W. Jiang, G. Zhu, X. Qian, Y. Fan, J. Yang, W. Luo, *Front. Chem.* **2019**, *7*, 266; e) W.-H. Ryu, H. Wilson, S. Sohn, J. Li, X. Tong, E. Shaulsky, J. Schroers, M. Elimelech, A. D. Taylor, *ACS Nano* **2016**, *10*, 3257; f) Y. Cui, K. Xiao, N. M. Bedford, X. Lu, J. Yun, R. Amal, D.-W. Wang, *Adv. Energy Mater.* **2019**, *9*, 1902148.

[12] a) S.-H. Cho, K. R. Yoon, K. Shin, J.-W. Jung, C. Kim, J. Y. Cheong, D.-Y. Youn, S. W. Song, G. Henkelman, I.-D. Kim, *Chem. Mater.* **2018**, *30*, 5941; b) K. R. Yoon, J. Choi, S.-H. Cho, J.-W. Jung, C. Kim, J. Y. Cheong, I.-D. Kim, *J. Power Sources* **2018**, *380*, 174; c) M. Karuppannan, Y. Kim, S. Gok, E. Lee, J. Y. Hwang, J.-H. Jang, Y.-H. Cho, T. Lim, Y.-E. Sung, O. J. Kwon, *Energy Environ. Sci.* **2019**, *12*, 2820; d) M. Kim, C. Kwon, K. Eom, J. Kim, E. Cho, *Sci. Rep.* **2017**, *7*, 44411.

[13] a) C. Wang, C. Shao, Y. Liu, X. Li, *Inorg. Chem.* **2009**, *48*, 1105; b) S.-C. Shen, W. K. Ng, Z.-Y. Zhong, Y.-C. Dong, L. Chia, R. B. H. Tan, *J. Am. Ceram. Soc.* **2009**, *92*, 1311.

[14] R. Sui, A. S. Rizkalla, P. A. Charpentier, *Langmuir* **2005**, *21*, 6150.

[15] a) T. Minasyan, L. Liu, M. Aghayan, M. A. Rodriguez, S. Aydinyan, I. Hussainova, *Prog. Nat. Sci.: Mater. Int.* **2019**, *29*, 190; b) R. R. Poolakkandy, M. M. Menamparambath, *Nanoscale Adv.* **2020**, *2*, 5015; c) K. R. Yoon, J.-W. Jung, I.-D. Kim, *ChemNanoMat* **2016**, *2*, 616.

[16] K. R. Yoon, J. W. Ko, D.-Y. Youn, C. B. Park, I.-D. Kim, *Green Chem.* **2016**, *18*, 944.

[17] H. Xu, J. Gao, M. Li, Y. Zhao, M. Zhang, T. Zhao, L. Wang, W. Jiang, G. Zhu, X. Qian, *Front. Chem.* **2019**, *7*, 266.

[18] F. Liu, X. Chen, Q. Xia, L. Tian, X. Chen, *RSC Adv.* **2015**, *5*, 77423.

[19] a) F. Y. Xie, L. Gong, X. Liu, Y. T. Tao, W. H. Zhang, S. H. Chen, H. Meng, J. Chen, *J. Electron Spectrosc. Relat. Phenom.* **2012**, *185*, 112; b) S. L. Wang, Y. L. Mak, S. Wang, J. Chai, F. Pan, M. L. Foo, W. Chen, K. Wu, G. Q. Xu, *Langmuir* **2016**, *32*, 13046; c) S. Y. Lee, G. Shim, J. Park, H. Seo, *Phys. Chem. Chem. Phys.* **2018**, *20*, 16932.

[20] J. Zhang, R. Yin, Q. Shao, T. Zhu, X. Huang, *Angew. Chem., Int. Ed.* **2019**, *58*, 5609.

[21] a) J. Li, H. Zhou, H. Zhuo, Z. Wei, G. Zhuang, X. Zhong, S. Deng, X. Li, J. Wang, *J. Mater. Chem. A* **2018**, *6*, 2264; b) D. Matthey, J. G. Wang, S. Wendt, J. Matthiesen, R. Schaub, E. Lægsgaard, B. Hammer, F. Besenbacher, *Science* **2007**, *315*, 1692; c) H.-H. Liu, Y. Wang, A.-P. Jia, S.-Y. Wang, M.-F. Luo, J.-Q. Lu, *Appl. Surf. Sci.* **2014**, *314*, 725.

[22] N. Zhang, D. Zhang, H. Chen, G. Wang, G. Yin, *Ionics* **2020**, *26*, 5697.

[23] a) Y. Sun, Y. Zong, J. Feng, X. Li, F. Yan, Y. Lan, L. Zhang, Z. Ren, X. Zheng, *J. Alloys Compd.* **2018**, *739*, 1080; b) A. Ruiz Puigdollers, P. Schlexer, S. Tosoni, G. Pacchioni, *ACS Catal.* **2017**, *7*, 6493.

[24] a) E. Sanville, S. D. Kenny, R. Smith, G. Henkelman, *J. Comput. Chem.* **2007**, *28*, 899; b) G. Henkelman, A. Arnaldsson, H. Jónsson, *Comput. Mater. Sci.* **2006**, *36*, 354; c) M. Yu, D. R. Trinkle, *J. Chem. Phys.* **2011**, *134*, 064111; d) W. Tang, E. Sanville, G. Henkelman, *J. Phys.: Condens. Matter* **2009**, *21*, 084204.

[25] A. Galyamova, K. Shin, G. Henkelman, R. M. Crooks, *J. Phys. Chem. C* **2020**, *124*, 10045.

[26] L. Sun, L. Zhou, C. Yang, Y. Yuan, *Int. J. Hydrogen Energy* **2017**, *42*, 15140.

[27] a) J. P. Perdew, K. Burke, M. Ernzerhof, *Phys. Rev. Lett.* **1996**, *77*, 3865; b) Y. Zhang, W. Yang, *Phys. Rev. Lett.* **1998**, *80*, 890.

[28] a) K. Locherer, I. Swainson, E. Salje, *J. Phys.: Condens. Matter* **1999**, *11*, 4143; b) T. Vogt, P. M. Woodward, B. A. Hunter, *J. Solid State Chem.* **1999**, *144*, 209.